ChemComm

COMMUNICATION

View Article Online
View Journal

Cite this: DOI: 10.1039/d4cc03193h

Received 28th June 2024,
Accepted 12th August 2024

DOI: 10.1039/d4cc03193h

rsc.li/chemcomm

Rationalising catalytic performance using a unique correlation matrix†

Maciej G. Walerowski, [a] Stylianos Kyrimis, [ab] Victoria A. Hewitt, [a] Lindsay-Marie Armstrong [b] and Robert Raja *[a]

Relationships between catalyst synthesis, structure and performance were investigated. Precise nanoparticle size control was achieved by tailoring solvent volume, drying temperature and solvent polarity. Catalyst performance was rationalised using a novel multidimensional correlation matrix, which considered synthetic, structural and catalytic data. This unique matrix can aid the design of improved catalysts.

The International Maritime Organization set an ambitious target of achieving net-zero for international shipping by 2050,[1] necessitating the development of sustainable marine fuels. Dimethyl ether (DME) is a viable alternative for marine diesel as it is non-toxic, compatible with existing liquid petroleum gas infrastructure and potentially a carbon-neutral fuel, as it can be produced *via* a circular carbon economy.[2,3] There are limited reports in the literature that outline the one-pot conversion of CO_2 to DME. One-pot DME synthesis is possible using a bifunctional catalyst which possesses redox sites for the hydrogenation of CO_2 into a methanol intermediate, and acidic sites for the subsequent dehydration of methanol to DME.[2–4] We recently reported the design and fabrication of a bifunctional catalyst, wherein SAPO-34 solid acid crystals were decorated with Cu^0–ZnO redox nanoparticles.[5] Whilst this bifunctional catalyst demonstrates comparable catalytic activity, it rivals other reported heterogeneous catalysts with its exceptional DME selectivity, and more importantly, no observable toxic CO byproduct formation. Cu^0–ZnO was chosen as a redox functionality as it shows good activity, is non-toxic, low-cost, widely studied, and is used in industrial applications.

The initial CO_2 hydrogenation step is thermodynamically challenging compared to the subsequent methanol dehydration step, indicating that the overall DME yield is limited by the activity of the redox sites.[2–4] Increasing redox site availability and accessibility is a potential method for improving the initial conversion of CO_2. This is possible by decreasing the redox nanoparticle size, which boosts the number of exposed active surface sites per gram of metal, thus improving the turnover frequency and metal utilisation.[6] Moreover, reducing nanoparticle size can further expose certain crystal facets which can influence product distribution.[6–8] For instance, it has been found that smaller Cu nanoparticles display higher methanol selectivity during CO_2 hydrogenation due to greater abundance of corner and edge sites.[8] Various methods have been applied to create and control the size and/or shape of Cu-based nanoparticles such as tailoring metal loading,[8–11] altering calcination procedures,[8,12] use of colloidal solutions,[13,14] specially designed reactors,[15] varying supports[10] and controlling reaction temperature.[16,17]

Although significant progress has been made in the synthesis of precisely-controlled nanoparticles,[6,7,18] studies often focus predominantly on the determination of nanoparticle shape and size and rarely consider the impact of their approach on other catalytically-relevant characteristics such as oxidation state and local structure. Treating nanoparticle shape and size as a sole descriptor of catalytic performance can lead to misleading structure–property correlations, as properties such as coordination number can change with nanoparticle modification. This highlights the need of multidimensional investigations, which couple synthetic variables, structural properties and catalytic performance to provide a more comprehensive understanding of features that can be tailored to give highly active and/or selective catalysts.

In this work, a series of bifunctional CO_2 to DME Cu^0–ZnO/SAPO-34 catalysts were synthesised using an impregnation approach, as this method was found to yield highly selective catalysts compared to other synthesis techniques.[5] Specifically, we investigated the impacts of changing solvent volume, drying temperature, solvent polarity and metal loading (Fig. S1, ESI†) on, firstly, the nanoparticle size and secondly on the overall catalyst structure & performance. Using the acquired data, we devised a unique and novel synthesis–structure–performance correlation (SSPC) matrix. Our SSPC matrix simultaneously showcases the impact of synthesis modification, not only on nanoparticle size, but also on oxidation

[a] School of Chemistry, University of Southampton, Southampton, SO17 1BJ, UK. E-mail: R.Raja@soton.ac.uk
[b] School of Engineering, University of Southampton, Southampton, SO17 1BJ, UK

† Electronic supplementary information (ESI) available. See DOI: https://doi.org/10.1039/d4cc03193h

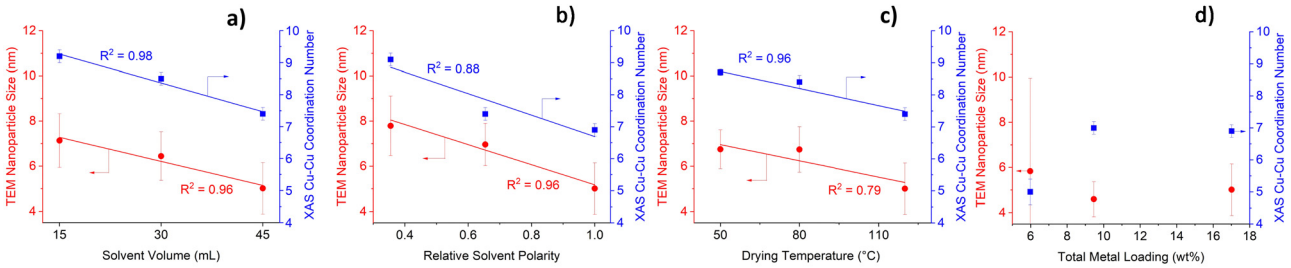

Fig. 1 Impact of (a) solvent volume (b) solvent polarity (c) drying temperature and (d) metal loading on TEM-derived nanoparticle size and XAS-derived Cu–Cu coordination number.

state, local structure, coordination geometry and catalytic performance. This has not been achieved by previous studies, to the best of our knowledge. This facilitates the creation of robust structure–property correlations, which aids model-based engineering of precisely-controlled catalysts. Full synthetic, characterisation & catalytic protocols can be found in Sections S1, S2 and S3 of the ESI,† respectively. We used a previously developed multidimensional analytical model to obtain the SSPC matrix and a full description of this model can be found in Kyrimis *et al.*[19]

Solvent volume, solvent polarity and drying temperature have a pronounced influence on TEM-derived nanoparticle sizes (Fig. 1 and Fig. S2, S3, ESI†). Increasing solvent volume and solvent polarity (Fig. 1a and b, respectively) yields Cu^0–ZnO/SAPO-34 bifunctional catalysts with smaller nanoparticles, which is likely due to more extensive dissolution of the Cu and Zn salts. This lowers localised precursor concentration, which reduces the likelihood of nuclei collisions and hence agglomeration.[15] Higher drying temperatures were also found to yield smaller nanoparticles (Fig. 1c). This is due to an increase in the rate of drying and impregnation, which indicates that the rate of nucleation is higher than the rate of nanoparticle growth, thus resulting in smaller nanoparticles.[20] To validate the TEM-derived nanoparticle sizes, the catalysts were characterised using XAS. Cu–Cu coordination numbers (CNs) can be obtained by fitting EXAFS results (Table S1, ESI†), which can signify nanoparticle size with lower Cu–Cu CNs, suggesting smaller nanoparticles.[21] The XAS Cu–Cu CNs (Fig. 1 and Fig. S4, ESI†) follow the same trend as TEM nanoparticle sizes, with both showing highly linear correlations between the synthetic variable of interest and the observed results. Precise control of nanoparticle size is thus possible by simply tailoring the solvent volume, solvent polarity or drying temperature. Our methodology aligns with green chemistry principles, as nanoparticle size modification can be achieved at mild temperatures, using no toxic solvents or additional reagents. Modifying solvent volume gives the most accurate control of nanoparticle size, as highly linear correlations are obtained using both TEM and XAS results. Fig. 1d shows a lack of linear correlation between metal loading and either nanoparticle size or Cu–Cu CNs. An inverse trend to nanoparticle size is observed for Cu oxidation state (OS), with high solvent volume, polarity, drying temperature, and low metal loading yielding higher Cu OS and Cu–O CN (Fig. S5 and Table S1, ESI†). The Cu OS correlates to Cu–Cu CN and to nanoparticle size (Fig. S6, ESI†). Smaller nanoparticles possess a greater surface-to-bulk ratio with a larger fraction of undercoordinated surface atoms, which will be more prone to forming a surface oxide.[6] This justifies the positive correlation between smaller nanoparticles and higher oxidation states. In contrast to the Cu centre, neither the Zn CN (Table S2, ESI†) nor Zn OS (Table S3, ESI†) is impacted significantly by the synthetic variables.

Solvent volume, solvent polarity and drying temperature had no significant impact on metal loading with all catalysts exhibiting similar Cu (~12 wt%) and Zn (~6 wt%) loadings with the expected 2 : 1 Cu/Zn mass ratio (Table S4, ESI†). Reducing intended loading lowers the actual metal loading as predicted. Cu(111) and Cu(200) XRD reflections were observed for all catalysts following the deposition of Cu and ZnO onto SAPO-34 crystals (Fig. S7, ESI†). ZnO reflections were not observed for any catalysts indicating the formation of either highly dispersed nanocrystallites or an amorphous ZnO phase. Only metal loading had a compelling impact on the XRD patterns, with weaker Cu(111) and Cu(200) reflections being observed for catalysts with lower loadings, which is expected. Solvent volume, drying temperature and solvent polarity had no significant influence on the total surface area of the Cu^0–ZnO/SAPO-34 catalysts, with BET surface areas ranging between 292 and 335 $m^2\ g^{-1}$ (Table S5, ESI†). In contrast, metal loading had a pronounced impact on surface area (303–397 $m^2\ g^{-1}$, Fig. S8, ESI†).

Kyrimis *et al.* investigated the correlation between reactor length & diameter, pressure drop, maximum temperature and methanol yield using a 3D response surface model.[19] The 3D response surface showcased how changes in input parameters (*i.e.*, reactor design) affected the output parameters (*i.e.*, reactor behaviour). As a proof of concept, we utilised the same method to model the influence of synthetic variables on predicted catalyst performance. Fig. 2a and Fig. S9 (ESI†) demonstrate the correlation between solvent volume, drying temperature, solvent polarity, and predicted DME metal time yield (MTY). Catalysts prepared using high solvent volume and drying temperature are estimated to show the highest activity and can achieve yields of over 300 $g_{DME}\ kg_{Metal}^{-1}\ h^{-1}$. In contrast, solvent polarity has a lesser impact on predicted yields. Experimental DME yields increased with metal loading as expected (Fig. S10, ESI†). Maximum DME selectivity is predicted by the model for catalysts synthesised using high volumes of low polarity solvents and high drying temperatures (Fig. 2b and Fig. S11, ESI†).

The developed model also allows us to establish multidimensional matrices to evaluate the association between

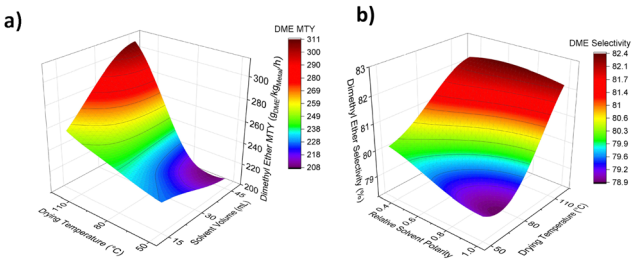

Fig. 2 Three-dimensional response surface model showing the impact of (a) drying temperature and solvent volume on predicted DME metal time yield and (b) relative solvent polarity and drying temperature on predicted DME selectivity.

investigated input and output parameters. Positive numbers (red) indicate that as an input parameter increases so does the output parameter, while negative numbers (blue) indicate the contrary. Magnitude shows the strength of correlation, with ±1 demonstrating strong correlation between an input and output parameter and smaller numbers indicating weak correlation. These correlations are presented in Tables 1 and 2, with Table 1 focusing on the correlation between experimental synthesis procedure and catalyst structure and Table 2 coupling experimental catalyst structure and performance. Table 1 confirms that increasing solvent volume, drying temperature or solvent polarity negatively influences, predominantly, the nanoparticle size and Cu–Cu CN, and positively influences the Cu–O CN and Cu OS. In other words, increasing these synthetic variables yields smaller, more oxidised nanoparticles. Solvent polarity impacts nanoparticle size most notably, with higher polarity solvents yielding smaller nanoparticles. Varying metal loading has a pronounced impact on all structural features once more highlighting that it is not a controlled method for tailoring nanoparticle size.

Focusing on the structure-performance correlation matrix (Table 2), it can be seen that increasing surface area and pore volume increases DME selectivity. Catalysts with higher surface areas will provide better access to internal acid sites of SAPO-34, which will increase the extent of methanol dehydration and hence DME selectivity. Decreasing nanoparticle size and Cu–Cu CN increases both the DME and methanol MTY, which can be rationalised by the fact that smaller nanoparticles will have more numerous surface active sites and hence more effectively catalyse the conversion of CO_2. Increasing Cu loading favours the formation of more methanol over DME. Higher Cu loading increases the number of active sites for conversion of CO_2 to methanol, but this increase comes at a cost of reducing acid site accessibility by the additional Cu^0 nanoparticles, which reduces the subsequent methanol dehydration. As such, there exists a trade-off between selectivity and activity by increasing loading.

Aside from activity and selectivity, stability is another key metric used to assess the overall catalyst performance. Fig. S7 (ESI†) shows a marginal increase in the intensity of the Cu(111) and Cu(200) XRD peaks, which can be attributed to minor sintering of nanoparticles, which is expected due to the significant water production during the reaction.[2] SAPO-34 contains some strong Brønsted acid sites, which can over dehydrate the intermediate methanol to coke, which can block the acid sites.[22] Fig. S7 (ESI†) demonstrates that coking has no detrimental impact on the CHA topology of SAPO-34, but does lower the surface area due to coke-induced pore clogging (Table S6, ESI†). DME MTY and selectivity have the most significant impact on the loss of surface area and hence on SAPO-34 deactivation. This is rationalised by the fact that catalysts displaying higher DME MTY and selectivity must have catalysed the dehydration of methanol to a greater extent and, as such,

Table 1 Synthesis–structure correlation matrix showing the impact of experimental synthetic variables on experimentally observed structural features. Bold font shows the experimental synthesis (input) parameters and normal font the observed structural (output) parameters

Parameter	**Solvent Volume**	**Solvent Polarity**	**Drying Temperature**	**Cu Intended Loading**	**Zn Intended Loading**	Surface Area	Pore Volume	Nanoparticle Size	Cu-Cu CN	Cu-O CN	Cu Actual Loading	Zn Actual Loading
Solvent Volume	1.0	0.0	0.0	0.0	0.0	0.1	0.3	-0.4	-0.5	0.4	-0.2	-0.2
Solvent Polarity	0.0	1.0	0.0	0.0	0.0	0.3	0.3	-0.7	-0.5	0.4	-0.1	-0.5
Drying Temperature	0.0	0.0	1.0	0.0	0.0	0.1	0.1	-0.2	-0.3	0.5	-0.3	-0.1
Cu Intended Loading	0.0	0.0	0.0	1.0	0.0	-0.2	-0.5	0.3	0.4	-0.4	0.4	0.5
Zn Intended Loading	0.0	0.0	0.0	0.0	1.0	-0.6	-0.6	0.2	0.4	-0.4	0.5	0.6
Surface Area	0.1	0.3	0.1	-0.2	-0.6	1.0	0.4	-0.2	-0.3	0.3	-0.2	-0.3
Pore Volume	0.3	0.3	0.1	-0.5	-0.6	0.4	1.0	-0.3	-0.4	0.4	-0.2	-0.4
Nanoparticle Size	-0.4	-0.7	-0.2	0.3	0.2	-0.2	-0.3	1.0	0.4	-0.4	0.2	0.4
Cu-Cu CN	-0.5	-0.5	-0.3	0.4	0.4	-0.3	-0.4	0.4	1.0	-0.5	0.3	0.4
Cu-O CN	0.4	0.4	0.5	-0.4	-0.4	0.3	0.4	-0.4	-0.5	1.0	-0.3	-0.4
Cu Actual Loading	-0.2	-0.1	-0.3	0.4	0.5	-0.2	-0.2	0.2	0.3	-0.3	1.0	0.3
Zn Actual Loading	-0.2	-0.5	-0.1	0.5	0.6	-0.3	-0.4	0.4	0.4	-0.4	0.3	1.0

Table 2 Structure–performance correlation matrix showing the impact of experimentally observed structural features on experimentally observed catalytic performance. Bold font shows the observed structural (input) parameters and normal font the observed catalytic performance (output) parameters

Name	Surface area	Pore volume	Nanoparticle Size	Cu-Cu CN	Cu-O CN	Cu Actual Loading	Zn Actual Loading	DME MTY	MeOH MTY	DME Selectivity	MeOH Selectivity	SA Loss
Surface area	1.0	0.4	-0.2	-0.3	0.3	-0.2	-0.3	0.0	-0.2	0.2	-0.2	0.4
Pore volume	0.4	1.0	-0.3	-0.4	0.4	-0.2	-0.4	0.1	-0.2	0.1	-0.1	0.0
Nanoparticle Size	-0.2	-0.3	1.0	0.4	-0.4	0.2	0.4	-0.3	-0.2	0.2	-0.2	0.0
Cu-Cu CN	-0.3	-0.4	0.4	1.0	-0.5	0.3	0.4	-0.2	-0.2	-0.1	0.1	0.0
Cu-O CN	0.3	0.4	-0.4	-0.5	1.0	-0.3	-0.4	0.0	0.1	0.0	0.0	-0.1
Cu Actual Loading	-0.2	-0.2	0.2	0.3	-0.3	1.0	0.3	0.1	0.4	-0.1	0.1	0.2
Zinc Actual Loading	-0.3	-0.4	0.4	0.4	-0.4	0.3	1.0	0.0	0.0	-0.1	0.1	-0.1
DME MTY	0.0	0.1	-0.3	-0.2	0.0	0.1	0.0	1.0	0.3	0.3	-0.3	0.3
MeOH MTY	-0.2	-0.2	-0.2	-0.2	0.1	0.4	0.0	0.3	1.0	0.1	-0.1	-0.1
DME Selectivity	0.2	0.1	0.2	-0.1	0.0	-0.1	-0.1	0.3	0.1	1.0	-1.0	0.2
MeOH Selectivity	-0.2	-0.1	-0.2	0.1	0.0	0.1	0.1	-0.3	-0.1	-1.0	1.0	-0.2
SA Loss	0.4	0.0	0.0	0.0	-0.1	0.2	-0.1	0.3	-0.1	0.2	-0.2	1.0

there is more opportunity for coke formation and hence deactivation. Catalyst stability is therefore explicitly linked to activity, with more active catalysts deactivating faster.

The proof of concept model described herein replicates experimental trends satisfactorily (Fig. S12 and Table S7, ESI†), validating its applicability. Improvements in catalyst and material design have often been achieved *via* laborious and time consuming trial and error approaches.[23] In the future, our model could be combined with datasets obtained using high throughput experimentation to provide a multidimensional perspective of the entire catalyst design space. This unique, multidimensional insight can help to uncover critical correlations, which can rationalise catalyst design strategies, resulting in rapid development of highly active and selective catalysts without the need for exhaustive testing.

To conclude, we have shown that precise control over nanoparticle size is possible by tailoring the solvent volume, solvent polarity, or drying temperature of the impregnation method. We have also developed a correlation matrix, as a proof of concept, which demonstrates that catalytic performance can be influenced by different structural factors at the same time, highlighting that, deriving structure–property correlations based on a narrow set of metrics can lead to erroneous insights.

We thank the University of Southampton and Southampton Marine and Maritime Institute for funding. We also thank the UK Catalysis Hub block allocation group for XAS beamtime (SP34632-1 and SP34632-2), Dr Matthew Cooper at the School of Ocean and Earth Science for help with ICP-MS analysis, and Regan Doherty at the University Hospital Southampton for help with TEM imaging.

Data availability

Data for this article, including raw characterisation and catalysis data are available from the University of Southampton repository at **https://doi.org/10.5258/SOTON/D3181**.

Conflicts of interest

There are no conflicts to declare.

Notes and references

1 International Maritime Organization, 2023 IMO Strategy on Reduction of GHG Emissions from Ships, 2023.
2 A. Ghosh, D. Nag, R. Chatterjee, A. Singha, P. S. Dash, B. Choudhury and A. Bhaumik, *Catal. Sci. Technol.*, 2024, **14**, 1387–1427.
3 J. Sun, G. Yang, Y. Yoneyama and N. Tsubaki, *ACS Catal.*, 2014, **4**, 3346–3356.
4 A. Álvarez, A. Bansode, A. Urakawa, A. V. Bavykina, T. A. Wezendonk, M. Makkee, J. Gascon and F. Kapteijn, *Chem. Rev.*, 2017, **117**, 9804–9838.
5 M. G. Walerowski, M. E. Potter, E. S. Burke, S. Kyrimis, L. M. Armstrong and R. Raja, *Catal. Sci. Technol.*, 2024, **14**, 3853–3863.
6 B. Roldan Cuenya and F. Behafarid, *Surf. Sci. Rep.*, 2015, **70**, 135–187.
7 B. R. Cuenya, *Acc. Chem. Res.*, 2013, **46**, 1682–1691.
8 L. Barberis, A. H. Hakimioun, P. N. Plessow, N. L. Visser, J. A. Stewart, B. D. Vandegehuchte, F. Studt and P. E. de Jongh, *Nanoscale*, 2022, **14**, 13551–13560.
9 A. Karelovic and P. Ruiz, *Catal. Sci. Technol.*, 2015, **5**, 869–881.
10 R. Van Den Berg, G. Prieto, G. Korpershoek, L. I. Van Der Waals, A. J. Van Bunningen, S. Lægsgaard-Jørgensen, P. E. De Jongh and K. P. De Jong, *Nat. Commun.*, 2016, **7**, 13057.
11 J. Kim, B. B. Sarma, E. Andrés, N. Pfänder, P. Concepción and G. Prieto, *ACS Catal.*, 2019, **9**, 10409–10417.
12 G. Prieto, J. Zečević, H. Friedrich, K. P. De Jong and P. E. De Jongh, *Nat. Mater.*, 2013, **12**, 34–39.
13 D. Mott, J. Galkowski, L. Wang, J. Luo and C. J. Zhong, *Langmuir*, 2007, **23**, 5740–5745.
14 M.-P. Pileni, *Nat. Mater.*, 2003, **2**, 145–150.
15 C. Ahoba-Sam, K. V. K. Boodhoo, U. Olsbye and K. J. Jens, *Materials*, 2018, **11**(1), 154.
16 M. A. Ben Aissa, B. Tremblay, A. Andrieux-Ledier, E. Maisonhaute, N. Raouafi and A. Courty, *Nanoscale*, 2015, **7**, 3189–3195.
17 H. Zhang, X. Ren, B. Zhang, A. Jia and Y. Wang, *ACS Appl. Mater. Interfaces*, 2023, **15**, 53515–53525.
18 T. S. Rodrigues, A. G. M. Da Silva and P. H. C. Camargo, *J. Mater. Chem. A*, 2019, **7**, 5857–5874.
19 S. Kyrimis, R. Raja and L. M. Armstrong, *Fuel*, 2024, **368**, 131511.
20 P. Munnik, P. E. De Jongh and K. P. De Jong, *Chem. Rev.*, 2015, **115**, 6687–6718.
21 A. M. Beale and B. M. Weckhuysen, *Phys. Chem. Chem. Phys.*, 2010, **12**, 5562–5574.
22 W. Dai, G. Wu, L. Li, N. Guan and M. Hunger, *ACS Catal.*, 2013, **3**, 588–596.
23 J. Li, Y. Sun and Z. Zhang, *SmartMat*, 2023, **4**, e1171.